

The oxygen-II luminosity density of the Universe¹

David W. Hogg^{2,3,4,5}, Judith G. Cohen³, Roger Blandford², Michael A. Pahre^{3,5,6}

ABSTRACT

Equivalent widths of [O II] 3727 Å lines are measured in 375 faint galaxy spectra taken as part of the Caltech Faint Galaxy Redshift Survey centered on the Hubble Deep Field. The sensitivity of the survey spectra to the [O II] line is computed as a function of magnitude, color and redshift. The luminosity function of galaxies in the [O II] line and the integrated luminosity density of the Universe in the [O II] line are computed as a function of redshift. It is found that the luminosity density in the [O II] line was a factor of ~ 10 higher at redshifts $z \sim 1$ than it is at the present day. The simplest interpretation is that the star formation rate density of the Universe has declined dramatically since $z \sim 1$.

Subject headings: galaxies: distances and redshifts — galaxies: evolution — galaxies: luminosity function, mass function — galaxies: statistics

1. Introduction

The [O II] line at 3727 Å is actually a pair of atomic transitions for singly ionized oxygen, the $^2D_{3/2}$ to $^4S_{3/2}$ at 3726 Å and the $^2D_{5/2}$ to $^4S_{3/2}$ at 3729 Å. The transitions are forbidden, meaning that there is no electric dipole connection between the initial and final states, so the spontaneous emission rates are small, 1.8×10^{-4} and $3.6 \times 10^{-5} \text{ s}^{-1}$ for the 3726 and 3729 Å transitions

¹ Based on observations made at the W. M. Keck Observatory, which is operated jointly by the California Institute of Technology and the University of California; at the Palomar Observatory, which is owned and operated by the California Institute of Technology; and with the NASA/ESA Hubble Space Telescope, which is operated by AURA under NASA contract NAS 5-26555.

² Theoretical Astrophysics, California Institute of Technology, mail code 130-33, Pasadena CA 91125, USA; rdb@tapir.caltech.edu

³ Palomar Observatory, California Institute of Technology, mail code 105-24, Pasadena CA 91125, USA; jlc@astro.caltech.edu

⁴ School of Natural Sciences, Institute for Advanced Study, Olden Lane, Princeton NJ 08540, USA; hogg@ias.edu

⁵ Hubble Fellow

⁶ Present address: Harvard-Smithsonian Center for Astrophysics, MS 20, 60 Garden St, Cambridge MA 02138, USA; mpahre@cfa.harvard.edu

respectively (Osterbrock 1989). For this reason, the [O II] line is usually collisionally excited by free electrons in hot nebulae; temperatures $T \sim 10^4$ K are needed to excite the 3.3 eV transitions. If the electron density is very low, collisional excitation is rare, whereas if it is very high, excited atoms are more likely to be deexcited by a subsequent collision than by spontaneous emission, so there are critical electron densities n_c at which the transitions saturate observationally, defined to be the electron densities at which the collisional excitation rates equal the spontaneous emission rates. The critical densities depend on temperature because the collisional excitation cross sections do, but at typical temperatures they are roughly 1.6×10^4 and 3×10^3 cm^{-3} for the 3726 and 3729 Å transitions respectively (Osterbrock 1989). (The fact that the two critical densities are different means that the 3726/3729 line ratio can be used to measure electron density.)

The conditions of temperature and density required to excite the [O II] 3727 Å line are met in H II regions, clouds of ionized hydrogen heated by massive, young, luminous stars. For this reason, the [O II] emission of a galaxy is sensitive to its young stellar population, or recent star formation history. In the local Universe, the relationship between [O II] luminosity and star formation has been calibrated

$$\frac{L_{[\text{O II}]}}{2 \times 10^{33} \text{ W}} = \frac{R}{1 \text{ M}_{\odot} \text{ yr}^{-1}} \quad (1)$$

where R is the star formation rate (Kennicutt 1992). This relationship shows a significant galaxy-to-galaxy scatter. It depends on galaxy dust content because dust absorbs strongly in the ultraviolet; the stellar initial mass function because the [O II] luminosity is tied only to the massive star population; and metallicity because the luminosity in the optically thin line ought to be proportional to oxygen abundance, which in turn depends on a galaxy’s age and star formation history.

In this study the [O II] luminosity function and [O II] luminosity density of the Universe are measured as a function of redshift. These functions constrain the star formation history of the Universe. Previous studies on the star formation history of the Universe have used the metal abundances in quasar absorption systems (Pei & Fall 1995) and broadband luminosity density (Lilly *et al.* 1996); both of these studies show a much higher star formation rate at $z \sim 1$ than at the present epoch. The star formation rate of the local Universe has been estimated through the luminosity density in the H α line (Gallego *et al.* 1995), which is a good measure of star formation rate (Kennicutt 1992). However, at redshifts $z > 0.3$ the H α line is no longer accessible by visual spectroscopy and therefore difficult to measure. The [O II] line is a less reliable measure of star formation rate (Kennicutt 1992) but it has the great advantage that it can be measured by visual spectroscopy over the interesting redshift range $0.3 < z < 1.3$ where the star formation rate density is thought to be changing rapidly. These considerations motivate the present work. Several recent studies have shown that the incidence of strong [O II] emission among bright galaxies increases with redshift (Cowie *et al.* 1996; Heyl *et al.* 1997; Small *et al.* 1997; Hammer *et al.* 1997). This trend implies a higher [O II] luminosity density in the past, which has also been previously measured directly (Hammer *et al.* 1997).

In what follows, physical quantities are quoted in SI units, with Hubble constant $H_0 = 100 h \text{ km s}^{-1} \text{ Mpc}^{-1}$, in world model $(\Omega_M, \Omega_\Lambda) = (0.3, 0)$. The only exception are number densities, which are given in $h^3 \text{ Mpc}^{-3}$. Fluxes and luminosities are given as flux and luminosity densities per logarithmic frequency interval, *i.e.*, νS_ν or λS_λ and νL_ν or λL_λ , in W m^{-2} and W . Luminosities are all-sphere (not per-steradian).

2. Sample, observations, and line measurement

The galaxy sample utilized for this study is an incompletely observed magnitude-limited sample, selected in the \mathcal{R} band, in the Hubble Deep Field (HDF, Williams *et al.* 1996) and an 8-arcmin diameter circular field surrounding it. The general sample selection, photometry and main spectroscopic results are described elsewhere (Hogg *et al.* in preparation; Cohen *et al.* in preparation). Briefly, the sample is selected to be all sources, independent of morphology, brighter than $\mathcal{R} = 23.3$ mag in the 8-arcmin diameter circular field and brighter than $\mathcal{R} = 24.5$ mag in the small HDF proper (most of the central $2 \times 2 \text{ arcmin}^2$). The spectroscopy of this sample is only about 75 percent complete for the purposes of this study, which is based on 375 spectra. (The redshift survey is more than 90 percent complete but some of the redshifts come from spectra taken by other groups.) Fluxes in the \mathcal{R} band and $\mathcal{R} - K_s$ colors are measured with data from the COSMIC and Prime Focus IR cameras on the Hale 200-inch Telescope (Kells *et al.* 1998). Spectroscopy is performed with the LRIS instrument on the Keck Telescope (Oke *et al.* 1995) with a 300 mm^{-1} grating, at a resolution of about 10 \AA (2.5 \AA per pixel, 1 arcsec slits), for exposure times of 6000 to 9000 s (Cohen *et al.* in preparation). Figure 1 shows some example spectra from the sample, cut out around the [O II] 3727 \AA line.

The continua are fit with a straight line over the wavelength range from 200 \AA to 50 \AA shortward of the observed 3727 location and the range from 50 \AA to 200 \AA longward. Each fit is performed with six iterations of sigma-clipping at $\pm 2.5\sigma$, where σ is the root-mean-square (RMS) residual noise per pixel. The uncertainty in the continuum value at the line center is taken to be the per-pixel RMS divided by the square root of the number of pixels contributing to the continuum fit (after sigma-clipping).

The line strength is measured by summing the differences between observed spectrum and continuum fit in the 30 \AA (full-width) aperture centered on the line location. The uncertainty in this strength is taken to be the per-pixel RMS times the square root of the number of pixels contributing to the line flux.

3. Equivalent width distributions

The rest-frame equivalent width W of a line in the spectrum of an object at redshift z is the wavelength interval of continuum which would provide the same total flux, corrected for redshift

$$W \equiv \frac{1}{1+z} \frac{\int [S_\lambda - S_\lambda^{(c)}] d\lambda}{S_\lambda^{(c)}} \quad (2)$$

where z is redshift, the integral is over only that spectral region which contains the line, S_λ is the flux density (per unit observed wavelength λ) and $S_\lambda^{(c)}$ is the flux density in the continuum at the location of the line; *i.e.*, the flux density which would be observed in the absence of the line. The equivalent width is a robust measure of the strength of a spectral feature relative to the source’s continuum measure; it does not depend on absolute calibration of the spectrum or even the relative calibration of different parts of the spectrum, as long as spectral response varies sufficiently slowly. It is a local, geometric measure of the line strength.

For the purposes of this study, the fractional uncertainty in an equivalent width measurement is taken to be the sum in quadrature of the fractional uncertainties in the continuum measurement and line strength, both described in the previous section. At low continuum signal-to-noise ratios, this is not strictly correct because the equivalent width error distribution is not gaussian or even symmetric around the measured value.

The rest-frame [O II] 3727 equivalent widths for the sample are shown in Figures 2 and 3, plotted against R -band magnitude and redshift z . Only spectra with good (signal-to-noise better than 2 in a pixel) continuum detections are plotted because badly estimated or zero continuum leads to large, unreliable equivalent width estimates. Figures 2 and 3 are encouraging for those undertaking faint galaxy redshift surveys because it shows that at higher redshifts and fainter fluxes, the equivalent widths of [O II] 3727 lines become greater. (The observed equivalent widths become even greater because of the additional factor of $[1+z]$.) Figures 2 and 3 are subject to an important selection effect: faint or high-redshift sources with small equivalent widths may simply not be successfully assigned a redshift at all. This selection effect can clear out the faint–small-width and high-redshift–small-width parts of these diagrams. However, the incompleteness in redshift identification is less than 10 percent for this sample (Cohen *et al.* in preparation). Furthermore, this selection effect does not explain any lack of observed objects at bright levels or low redshifts with large equivalent widths. One recent study shows a strong inverse correlation between galaxy luminosity and [O II] equivalent width (Cowie *et al.* 1996). That inverse correlation is not seen as strongly in the sample analyzed here, nor that of Small *et al.* (1997), especially when sources with low signal-to-noise continuum measurements are excluded (Small, private communication), as they have been in Figures 2 and 3. Because the equivalent width is a ratio of observed quantities, there is a tendency to overestimate the equivalent widths of lines in sources with low signal-to-noise continuum measurements.

Figure 2 may show evidence for clumps in redshift–equivalent-width space. The survey field

is only 8 arcmin in diameter, just a few Mpc at high redshift in typical models, so sources with similar redshifts are likely to be physically associated. This suggests that the galaxies which reside in the same high-redshift group may also be related in terms of stellar content. It suggests that at least some of the galaxies in each group formed at the same time and with similar stellar populations. This is nicely consistent with the observation that groups are long-lived, primordial structures which exist at high redshift in relatively high abundance (Cohen *et al.* 1996a, 1996b; Steidel *et al.* 1997).

4. Sensitivity to line emission

The identification of the line at redshift z depends on (a) the fraction of spectra in the sample which include wavelength $(3727 \text{ \AA})(1+z)$ in their spectral range, (b) the total sensitivity of the atmosphere plus telescope plus instrument to line flux at $(3727 \text{ \AA})(1+z)$, and (c) the accuracy to which night sky and other background emission can be subtracted at $(3727 \text{ \AA})(1+z)$. Because the spectrograph is a multi-slit design, different sources in the survey are observed over different wavelength ranges, depending on the position of the source within the field of the instrument. The wavelength coverage function can be constructed by taking the minimum and maximum possible source locations and assuming that on any given slitmask sources are evenly distributed between these extremes. The sensitivity to flux (in the sense of νS_ν) can be estimated with observations of spectrophotometric standard stars. The sensitivity varies from night to night, so in principle this function should be replaced with a distribution function which takes into account the variation in observing conditions. Furthermore, in the multislit design, if there are any positional errors in the catalog or mask misalignment while observing, different sources will be centered on their slits with different precisions. This leads to a random scatter in throughputs, even for sources observed simultaneously. The sky brightness, color and emission line spectrum also vary from night to night. In principle the expected sensitivity to 3727 emission can be estimated from the coverage, sensitivity, and sky brightness functions. However, because the sensitivity depends on data reduction technique, includes the complications of assessing slitmask alignment, and may be compromised by unknown instrumental effects, a purely empirical approach is taken here, using the reduced spectra themselves to assess the sensitivity.

The signal-to-noise ratio r (defined to be continuum level divided by pixel-to-pixel rms), is measured in every spectrum in the sample at a set of wavelengths corresponding to the 3727 line at various redshifts in the range $0 < z < 1.8$, by exactly the procedure used to estimate the continuum in the equivalent width measurements described above. The rms is computed from only those pixels not rejected by the sigma-clipping algorithm, which is perhaps optimistic. These continuum signal-to-noise ratios are “scaled” to the value they would have if the source had $\mathcal{R} = 23$ mag and a spectral exponent $n = 0$ (the spectral exponent n used in this work is defined by $\nu S_\nu \propto \nu^n$ and it is measured from the $\mathcal{R} - K_s$ color). This scaling is done by multiplying the

measured signal-to-noise ratio by

$$\begin{aligned} & 10^{0.4(\mathcal{R}-23)} \left(\frac{1+z}{1.85} \right)^n & \text{if } \mathcal{R} > 21.5 \text{ mag} \\ & 10^{0.4(-1.5)} \left(\frac{1+z}{1.85} \right)^n & \text{if } \mathcal{R} < 21.5 \text{ mag} \end{aligned} \quad (3)$$

where the switch-over at $\mathcal{R} = 21.5$ mag takes place because at fainter magnitudes most of the source is in the slit and intensity through the slit is proportional to total source flux, while brighter than that the source is typically larger than the slit and intensity through the slit depends only weakly on total source flux since the bright galaxies in the sample have similar surface brightnesses. The $1+z$ term is divided by 1.85 because $z = 0.85$ puts 3727 into the center of the \mathcal{R} band. The switch-over magnitude was determined by trial-and-error, with the test being that the distribution of scaled signal-to-noise ratios not depend strongly on magnitude. The signal-to-noise ratio can be converted into a sensitivity to rest-frame equivalent width, expressed in terms of the smallest detectable rest-frame equivalent width

$$W_{\text{lim}} = \frac{\eta \lambda_1}{r} \left(\frac{\Delta\lambda}{\lambda_1} \right)^{1/2} (1+z)^{-1/2} \quad (4)$$

where η is the minimum necessary signal-to-noise ratio for 3727 to be detected, taken to be 3, r is the scaled signal-to-noise ratio in the continuum, λ_1 is the wavelength per pixel, usually 2.5 \AA for these spectra, $\Delta\lambda$ is the rest-frame full-width of the 3727 line, taken to be 10 \AA , and z is the redshift. Because the formula for W_{lim} includes r in the denominator, the scaled value can be converted back into the true sensitivity to rest-frame equivalent width by multiplying by the factors given in (3).

Since the continuum of every spectrum is measured at every redshift, there are a huge number of scaled W_{lim} estimates from which a model of the spectrograph sensitivity can be constructed. At each redshift the scaled sensitivities are ranked and a cumulative distribution is constructed. This distribution is shown in Figure 4. The distribution is plotted cumulatively so that it can be treated as a probability, given a source with a given redshift and [O II] equivalent width, that the line is detected.

Note that this sensitivity function is empirical, derived from the sample of spectra themselves, and is only valid for this survey, because it depends on the instrument, site, observational technique, reduction method, and selection function. The sensitivity becomes worse at redshifts $1 < z < 1.25$ because the CCD efficiency at the relevant wavelength is dropping while the sky brightness and number of bright night sky emission lines are both increasing, and then very bad at redshifts $1.25 < z < 1.5$ because in addition the fraction of spectra with coverage at long enough wavelength is also decreasing. Similarly, the bad sensitivity to [O II] emission at low redshifts $z < 0.3$ is also caused by a decreasing fraction of spectra with coverage at short enough wavelengths (although at these low redshifts other spectral features can be used to determine redshifts).

5. The [O II] luminosity function

For any galaxy, the line luminosity $L_{[\text{O II}]}$ can be crudely computed with the rest-frame equivalent width W , the flux S (defined to be νS_ν) and the spectral exponent n (defined so $\nu S_\nu \propto \nu^n$) by

$$\log L_{[\text{O II}]} = \log \left[\frac{W}{3727 \text{ \AA}} \right] + \log S + \log[4\pi] + 2 \log D_L(z) - n \log \left[(1+z) \frac{3727 \text{ \AA}}{\lambda_{\mathcal{R}}} \right] \quad (5)$$

where $D_L(z)$ is the luminosity distance in an $(\Omega_M, \Omega_\Lambda) = (0.3, 0.0)$ universe, and $\lambda_{\mathcal{R}}$ is the effective wavelength of the \mathcal{R} band, or 6900 Å. Note that this is an all-sphere (not per-steradian) luminosity definition. Fluxes are derived from \mathcal{R} -band magnitudes using a standard absolute calibration (Steidel & Hamilton 1993). This prescription for line luminosity is crude because the spectral energy distributions of galaxies are not pure power-laws, and, furthermore, in this study, the spectral exponent n has been computed from the $\mathcal{R} - K_s$ color, which does not “bracket” the [O II] line unless the redshift is $z > 0.85$. A refinement would be to compute n from, say, $G - \mathcal{R}$ at redshifts $z < 0.85$. In principle the need to use the flux S and exponent n can be obviated entirely because line fluxes can be measured directly from spectrophotometric data. However, such procedures depend on perfect slit alignment on the galaxies and aperture corrections to account for line flux outside the slit. The procedure used here is more robust.

The luminosity function is estimated with a modified version of the $\langle V/V_{\text{max}} \rangle$ method, in which each galaxy in the survey is assigned a volume V_{max} which is the volume of the Universe in which that source could lie and still meet the survey criteria. The inverse volumes of all the galaxies in a particular luminosity bin are summed to estimate the luminosity function in that bin. In this application, there are two important complications in computing V_{max} . The first is that the survey is incomplete, in the sense that only about 75 percent of the sources in the field are observed as part of the subsample used here. Figure 5 shows the *a priori* completeness function, which is defined to be the fraction of the total sources in the field which were observed spectroscopically, as a function of \mathcal{R} -band flux. The second complication is that whether or not a source is in the sample depends not only on the *a priori* completeness function but also on the detection of the [O II] line itself, both because if it is not detected there is no luminosity (for the luminosity function) and because redshift identification often depends on [O II] detection anyway. Fortunately, however, the sensitivity to the [O II] line is computed in Section 4 and shown in Figure 4. Recall that the plotted sensitivity function is scaled to an equivalent $\mathcal{R} = 23$ mag, $n = 0$ source by the scaling given in (3); the scaling and the function in Figure 4 can be combined to make a total probability $p_{\text{detect}}(S, n, z, W)$ of detecting an [O II] line of equivalent width W in a source with flux S , spectral exponent n and redshift z .

Given the completeness function and detection probability function, the appropriate formula for each galaxy’s volume V_{max} is

$$V_{\text{max}} = \int_0^\infty \eta_{\text{try}}(S') p_{\text{detect}}(S', n, z', W) \frac{d^2 V_{z'}}{d\Omega dz'} \Delta\Omega dz' \quad (6)$$

where $\eta_{\text{try}}(S)$ is the probability that a spectrum was taken of a source of flux S in an attempt to get its redshift, and S' is the flux the source would have if it were at redshift z' rather than its true redshift. The function η_{try} is plotted for this spectroscopic sample in Figure 5. The luminosity function $\phi(\log L_i)$ (number density per logarithmic interval in luminosity) in a bin of [O II] luminosity width $\Delta \log L$ centered on [O II] luminosity $L_{[\text{O II}]} = L_i$ is estimated with

$$\phi(\log L_i) = \frac{1}{\Delta(\log L)} \sum_{|\log L_{[\text{O II}],j} - \log L_i| < \Delta(\log L)/2} \frac{1}{V_{\text{max},j}} \quad (7)$$

where the sum is over all galaxies with luminosities in the bin, so index i labels luminosity bins and index j labels galaxies. Variances are computed by summing the squares of the inverse volumes; the error bars on the Figures are the root variances.

The [O II] luminosity function is shown in Figure 6 for the entire sample, in the redshift range $0 < z < 1.5$. It is compared to the local H α luminosity function from the UCM survey (Gallego *et al.* 1995) where the H α points have been multiplied by a factor of 0.46, the mean observed [O II]/H α flux ratio in the local Universe (Kennicutt 1992). Figure 7 shows the luminosity for two subsamples split in redshift at $z = 0.35$. This Figure shows a strong evolution in the [O II] luminosity function at the bright end. Although the total number density of [O II]-emitting galaxies is not significantly different between the two subsamples, the typical line luminosity is higher by an order of magnitude in the higher-redshift subsample. Both subsamples show a higher line luminosity than that which would be predicted from the very local UCM results, given the local [O II]/H α flux ratio. Although there may be some bias against luminous, low-redshift sources due to undersampling, it is not strong enough to produce the apparent evolution shown in Figure 7, especially since (a) the undersampling is accounted-for with the *a priori* completeness function and (b) even the “low-redshift” sample goes to redshift $z = 0.35$, where there are many galaxies in the sample with luminosities around L^* .

6. The [O II] luminosity and star formation rate densities

As discussed in Section 1, the [O II] line luminosity is a star formation indicator, so the [O II] luminosity function is a measure of the star formation rate density of the Universe. For these purposes the entire luminosity function is not necessary, only the integrated luminosity density is needed. Because this is a single number rather than a function, it is possible to subdivide the sample more finely in redshift than was possible in Section 5.

The luminosity density $\mathcal{L}_{[\text{O II}]}$ in the [O II] line is estimated similarly to the luminosity function, using the same volumes V_{max} computed for those purposes. The integrated luminosity density is computed with

$$\mathcal{L}_{[\text{O II}]} = \sum_j \frac{L_{[\text{O II}],j}}{V_{\text{max},j}} \quad (8)$$

where galaxies are labeled by index j . The variance on this quantity is taken to be the Poisson value: the sum of the square contributions. The [O II] line luminosity density as a function of redshift, computed in two overlapping “binnings,” is shown in Figure 8, along with the local measurement of the H α luminosity density from the UCM survey, again scaled by the local [O II]/H α flux ratio. The random errors on the individual points in Figure 8 are in fact expected to be larger than the plotted poissonian uncertainties on account of the strong redshift clustering found in this and other small redshift survey fields (Cohen et al 1996b), in which more than 50 percent of sources are found to be concentrated into a few narrow redshift spikes out to $z \approx 1$. This is seen dramatically in the point at $z = 0.5$, which is high even relative to its overlapping neighbors; there are several large redshift overdensities in this $0.4 < z < 0.6$ bin. Unfortunately this is a single-field study and only when several independent fields have been similarly analyzed will it be possible to average out such field-to-field variations.

After accounting for differences in Hubble constant and world model, the luminosity density measurements shown in Figure 8 are in good agreement with those of Hammer et al (1997).

Figure 8 also shows the star formation rate density, computed from the luminosity density with the Kennicutt (1992) local calibration given by (1). Overall, Figure 8 implies that the star formation rate density was nearly ten times higher at $z \sim 1$ than at the present day. A full analysis must take account of the changing metal, gas, and dust contents of high-redshift galaxies, factors that are difficult to assess with confidence at the present time. Our results are consistent with star formation rate density estimates based on broadband luminosity density (Lilly et al 1996) and quasar absorption line metallicities (Pei & Fall 1995), both of which suggest factor-of-ten reductions from $z \sim 1$ to the present day.

The authors are pleased to thank Kurt Adelberger and Chuck Stiedel, who provided some of the imaging data used in this study, and Todd Small, Ed Groth, and the referee, David Spergel, for helpful comments on the manuscript. This research is based on observations made at the W. M. Keck Observatory, which is operated jointly by the California Institute of Technology and the University of California; at the Palomar Observatory, which is owned and operated by the California Institute of Technology; and with the NASA/ESA Hubble Space Telescope, which is operated by AURA under NASA contract NAS 5-26555. Financial support was provided under NSF grant AST 95-29170, Hubble Space Telescope archival research grant AR-06337.12-94A, and Hubble Fellowship grants HF-01093.01-97A and HF-01099.01-97A. The Hubble grants are provided by STScI, which is operated by AURA under NASA contract NAS 5-26555. This research made use of the NASA ADS Abstract Service and the SM software package.

REFERENCES

Cohen J. G., Hogg D. W., Pahre M. A. & Blandford R., 1996a, ApJ 462 L9

- Cohen J. G., Cowie L. L., Hogg D. W., Songaila A., Blandford R., Hu E. M. & Shopbell P., 1996b, ApJ 471 L5
- Cowie L. L., Songaila A., Hu E. M. & Cohen J. G., 1996, AJ 112 839
- Ellis R. S., Colless M., Broadhurst T., Heyl J. & Glazebrook K., 1996, MNRAS 280 235
- Gallego J., Zamorano J., Aragón-Salamanca A. & Rego M., 1995, ApJ 455 L1
- Glazebrook K., Ellis R., Colless M., Broadhurst T., Allington-Smith J. & Tanvir N., 1995b, MNRAS 273 157
- Hammer F., Flores H., Lilly S. J., Crampton D., Le Fèvre O., Rola C., Mallen-Ornelas G., Schade D. & Tresse L., 1997, ApJ 481 49
- Heyl J. S., Colless M., Ellis R. S. & Broadhurst T., 1997, MNRAS 285 613
- Kells W., Dressler A., Sivaramakrishnan A., Carr D., Koch E., Epps H., Paradillian G., & Hilyard D., 1998, PASP to be submitted
- Kennicutt R. C. Jr., 1992, ApJ 388 310
- Lilly S. J., Le Fèvre O., Hammer F. & Crampton D., 1996, ApJ 460 L1
- Oke J. B. *et al.*, 1995, PASP 107 375
- Osterbrock D. E., 1989, *Astrophysics of Gaseous Nebulae and Active Galactic Nuclei*, University Science Books, Mill Valley
- Pei Y. C. & Fall S. M., 1995, ApJ 454 69
- Small T. A., Sargent W. L. W. & Hamilton D., 1997, ApJ 487 512
- Steidel C. C. & Hamilton D., 1993, AJ 105 2017
- Steidel C. C., Adelberger K. L., Dickinson M., Giavalisco M., Pettini M. & Kellogg M., 1998, ApJ 492 428
- Williams R. E. *et al.*, 1996, AJ 112 1335

Jan 20 15:05:59 1998

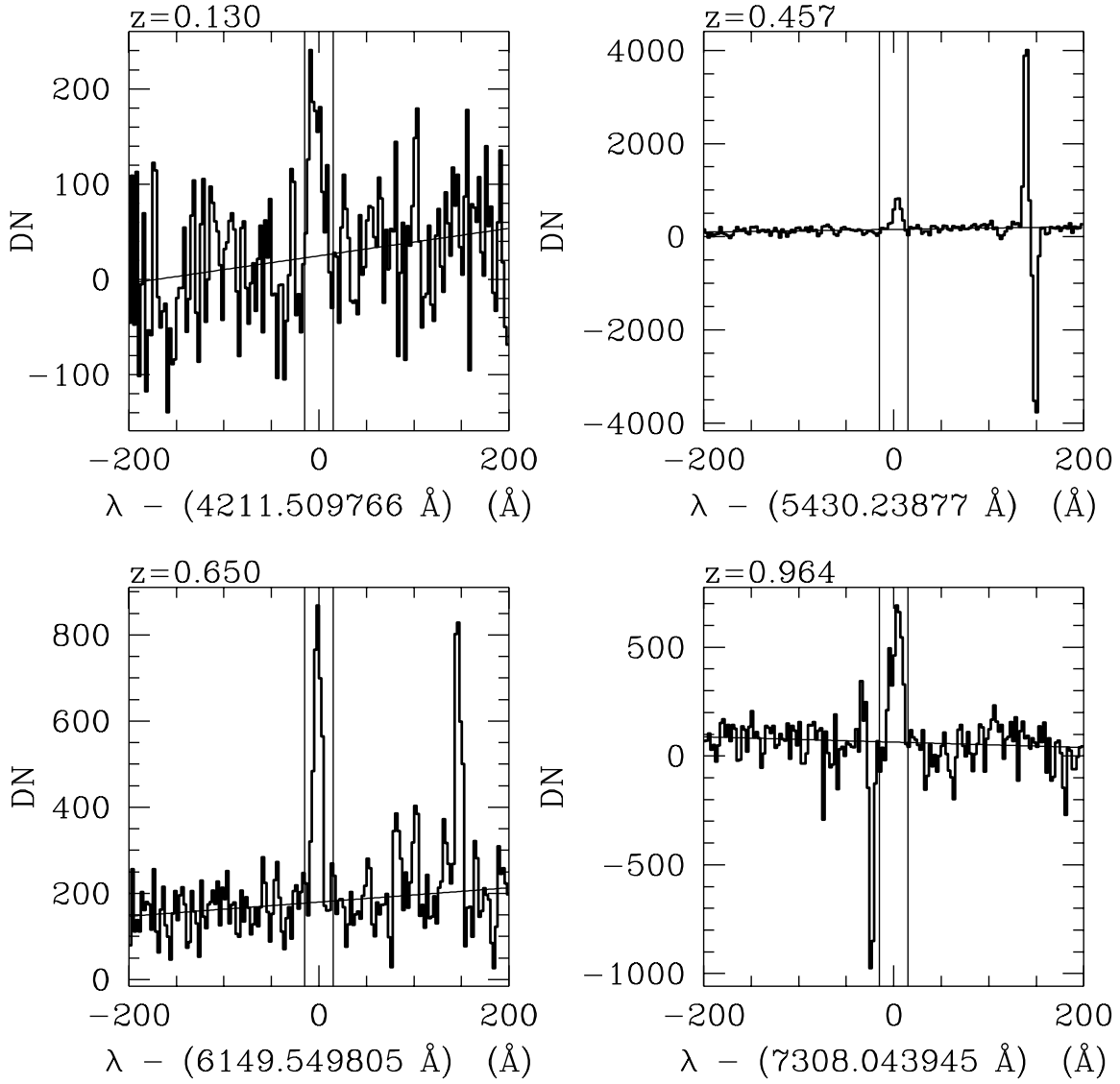


Fig. 1.— Example [O II] 3727 Å line detections for four sources from the sample. The data (in “data numbers” or DN) are shown with a dark line, the fit continuum with a thin straight line, and the aperture in which the 3727 line strength is measured with two thin vertical lines. The redshift of each source is given in the top left corner of each plot. Spikes or features not at zero wavelength are residuals of sky lines imperfectly subtracted.

Jan 20 15:06:16 1998

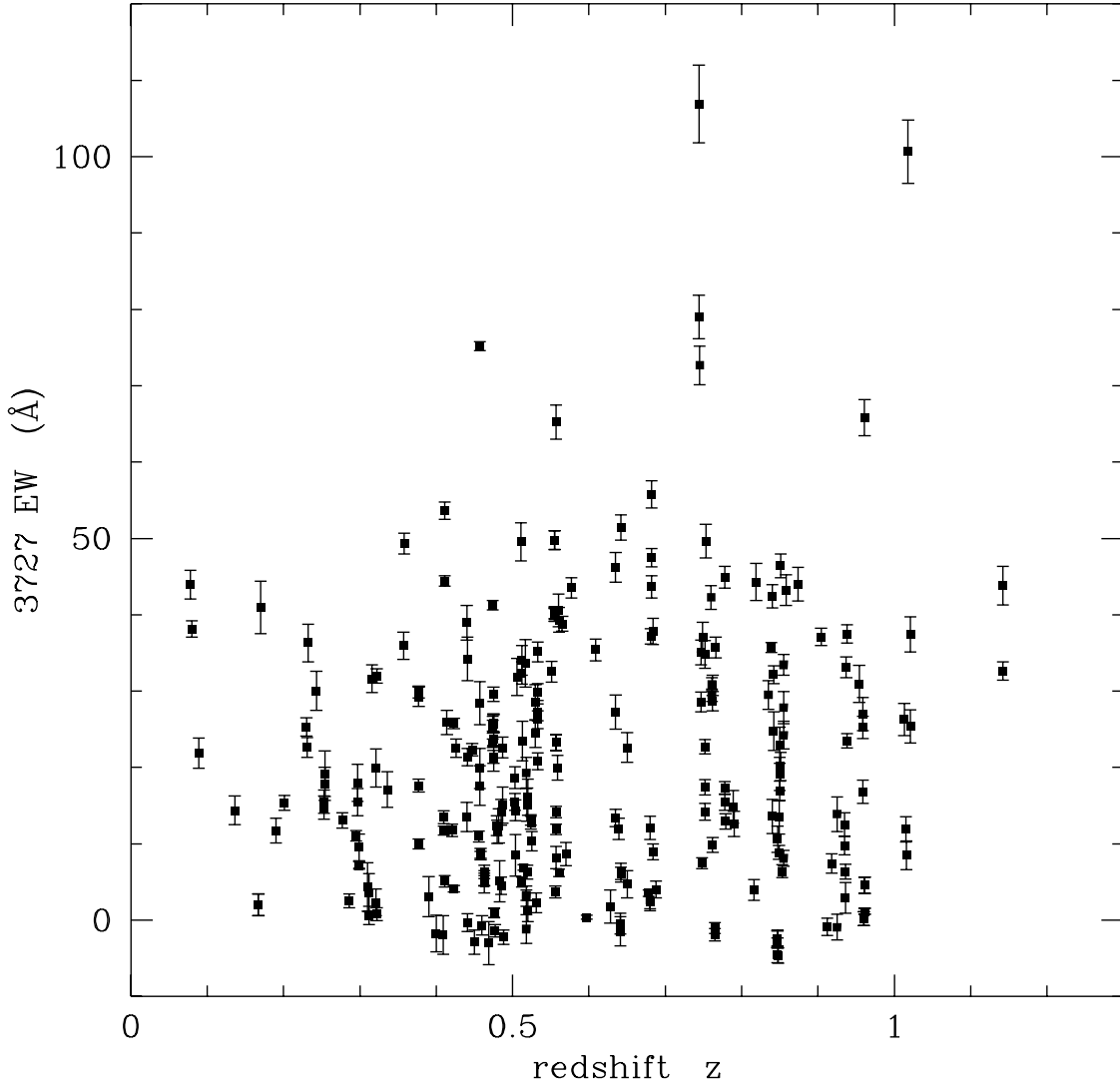


Fig. 2.— Rest-frame [O II] 3727 Å line equivalent widths plotted against redshift z . Only those spectra with continuum detections near rest-frame 3727 Å better than a signal-to-noise ratio of 2 (in one pixel) are plotted. Uncertainty estimates are described in Section 2. The error bars are all much smaller than 50 percent because the two-sigma limit on the continuum is a per-pixel limit, while in fact many pixels around 3727 were used to determine the continuum level, making the continuum measurement much more secure than two sigma.

Jan 20 15:06:24 1998

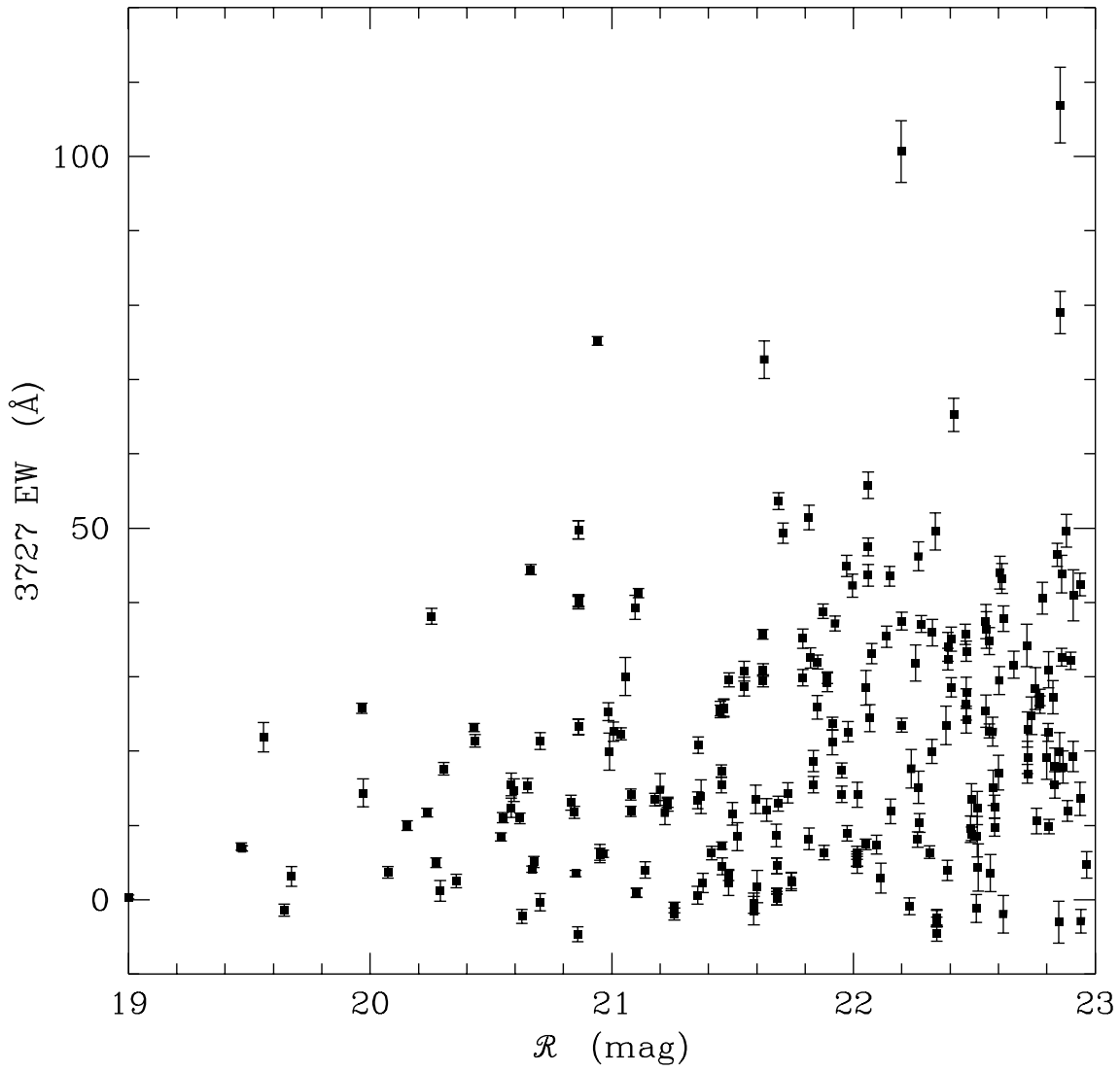


Fig. 3.— Rest-frame [O II] 3727 Å line equivalent widths plotted against \mathcal{R} -band apparent magnitude. Only those spectra with continuum detections near rest-frame 3727 Å better than a signal-to-noise ratio of 2 (in one pixel) are plotted. Uncertainty estimates are described in Section 2.

Jan 20 15:28:58 1998

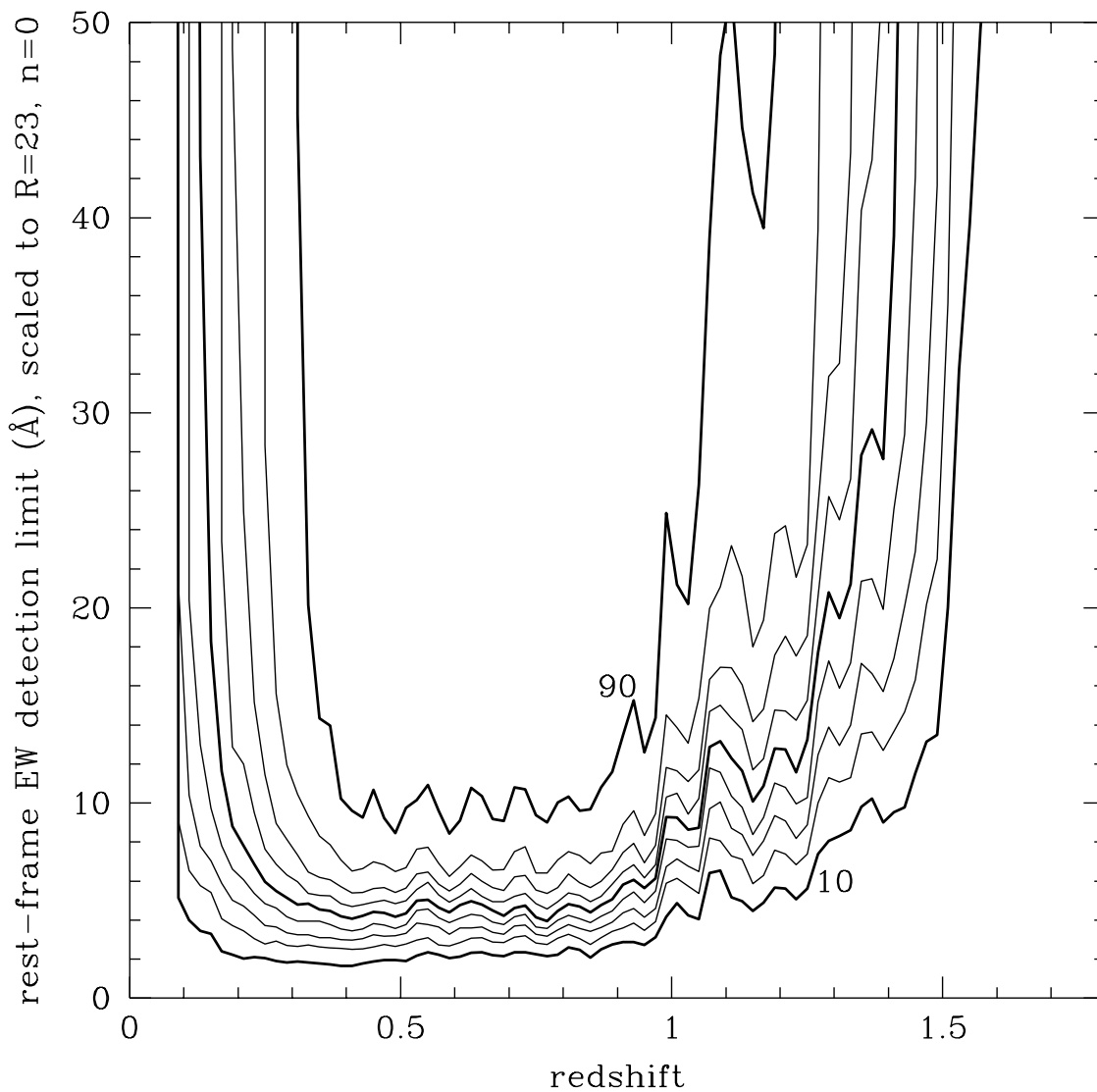


Fig. 4.— The cumulative distribution of scaled sensitivities to [O II] 3727 Å emission, in terms of rest-frame equivalent width. The dark lines are the 10, 50, and 90 percent contours and the thin lines are spaced by 10 percent. The sensitivities are scaled to $\mathcal{R} = 23$ mag and $n = 0$ (flat spectrum in νf_ν) as described in the text.

Jan 20 15:30:36 1998

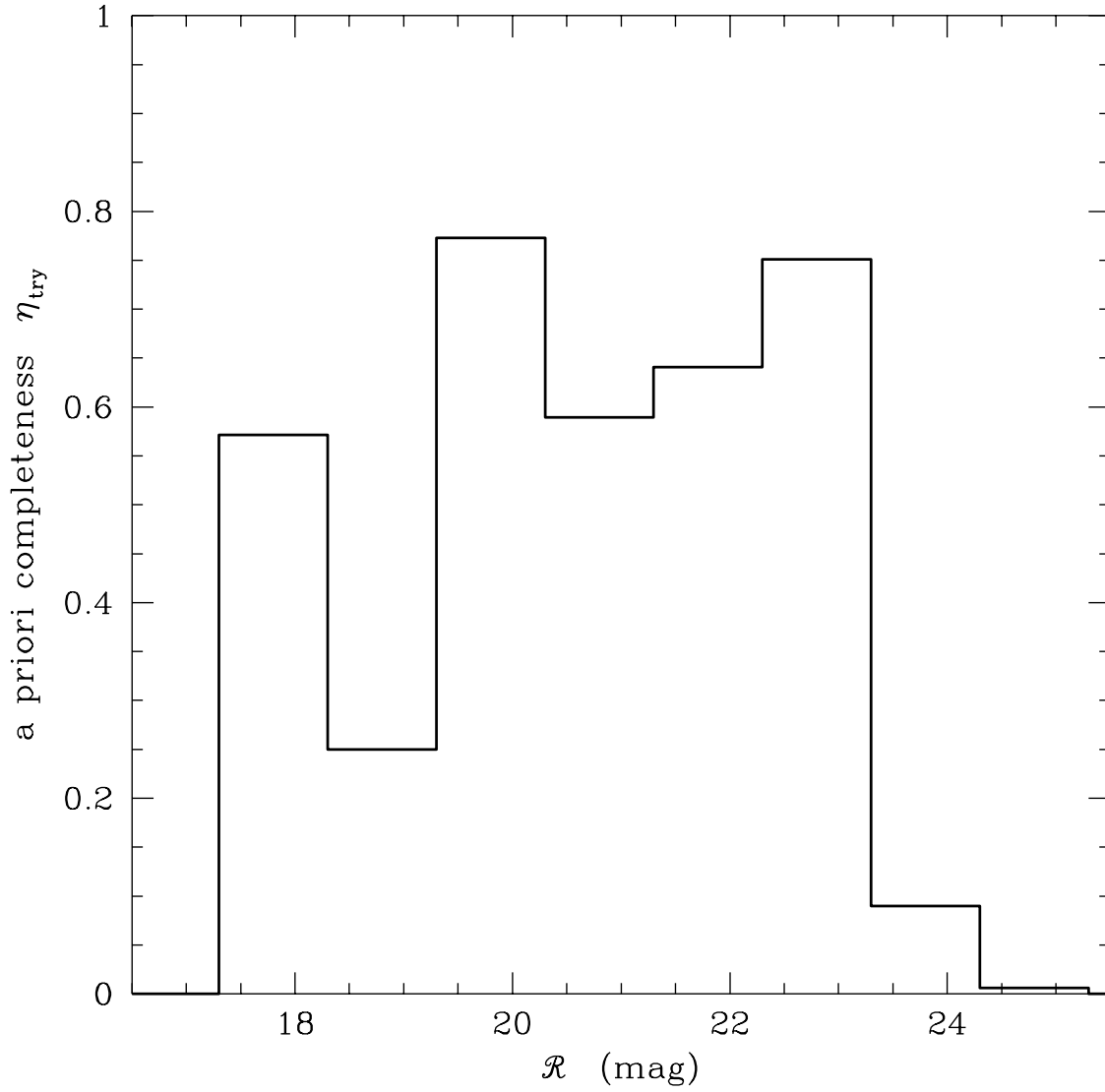
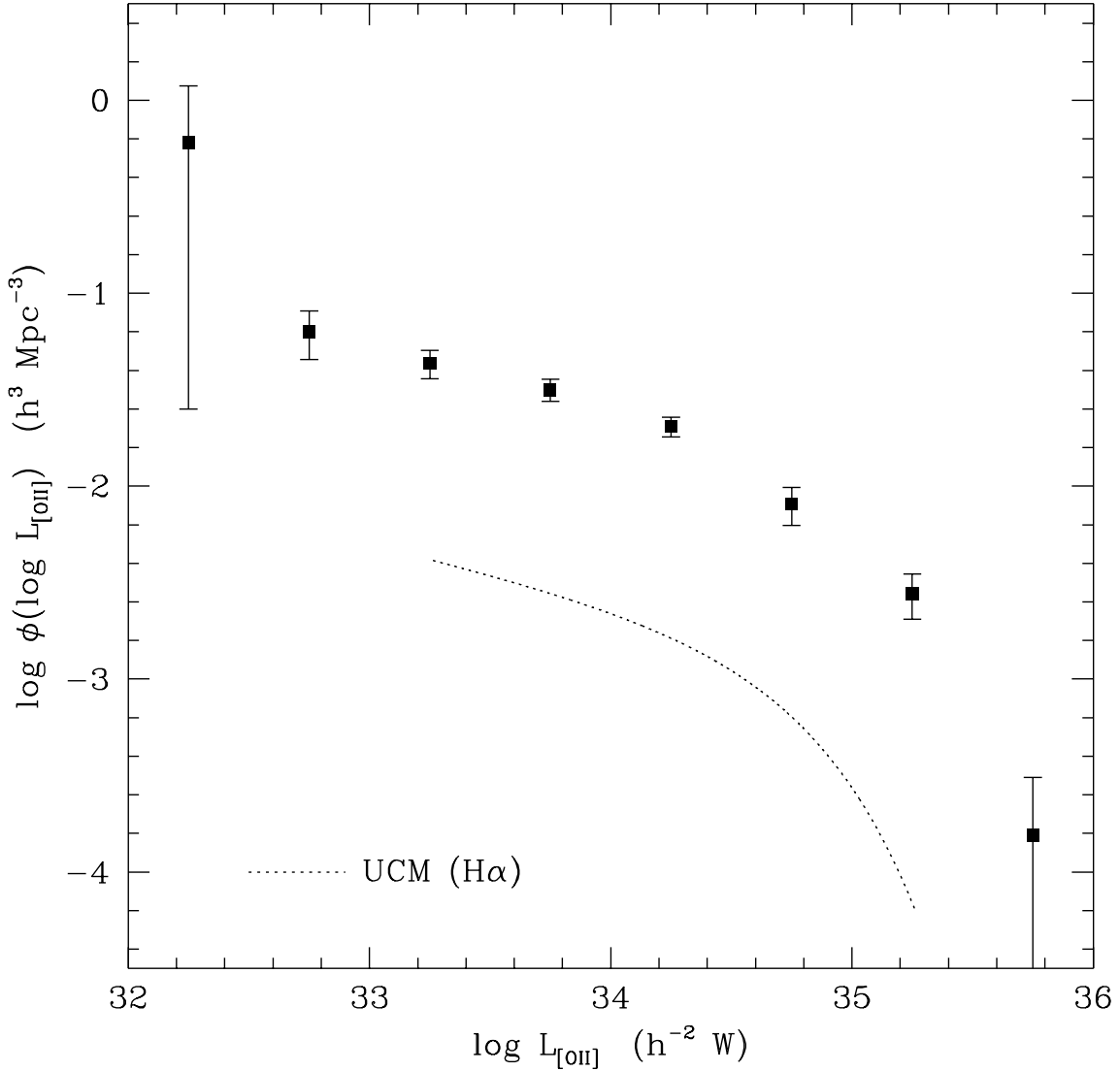
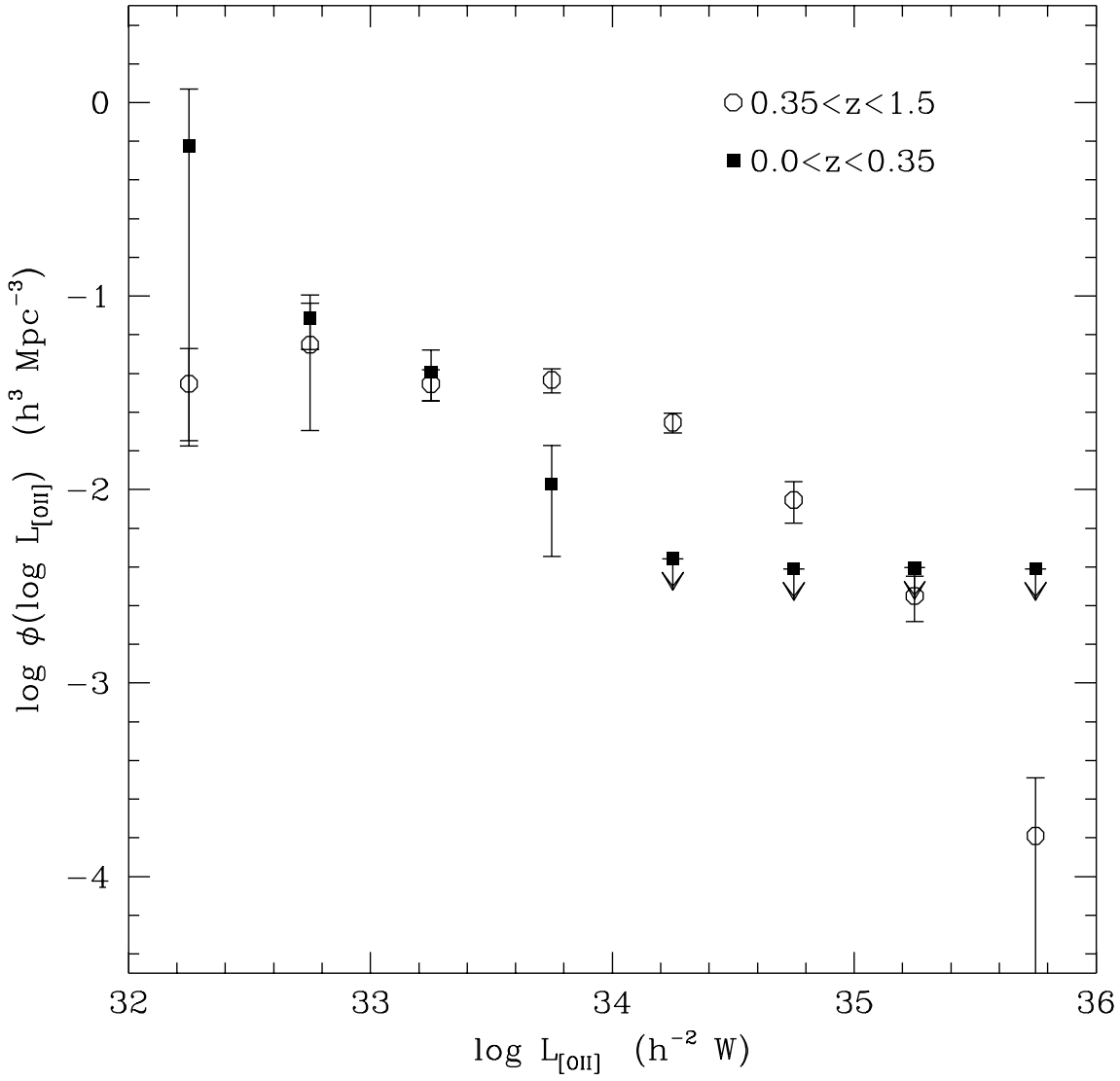


Fig. 5.— The probability, as a function of \mathcal{R} -band flux, that a source in the 8-arcmin diameter HDF sample was observed spectroscopically as part of this sample. *I.e.*, this function is the fraction of sources in the field which were observed spectroscopically. The completeness drops rapidly at $\mathcal{R} = 23.3$ mag because observations fainter than this were only performed in the central, HST-imaged, 5 arcmin² of the field.



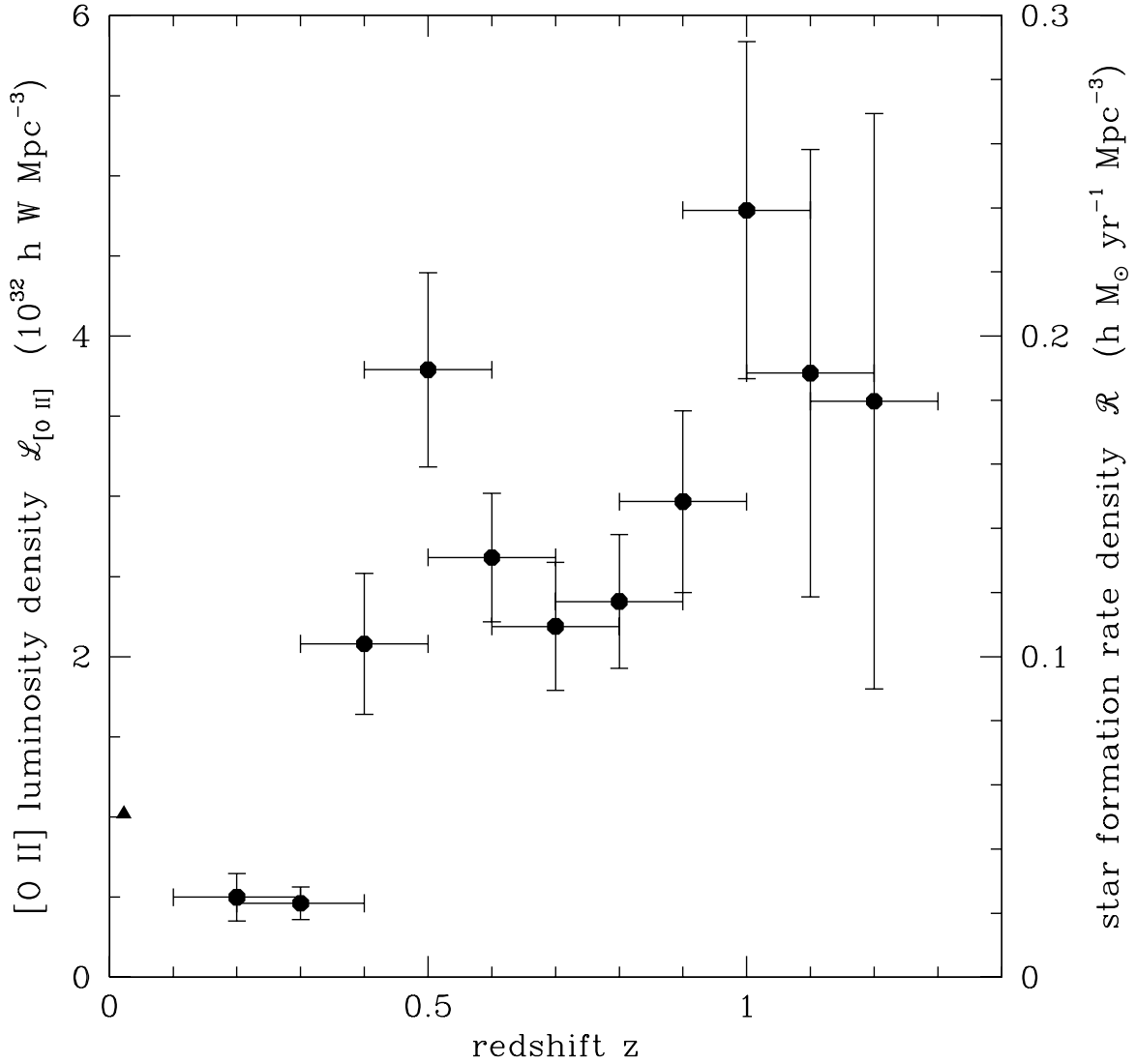
Feb 16 17:25:07 1998

Fig. 6.— The [O II] 3727 Å luminosity function, determined from the whole sample used in this Chapter. The luminosities, luminosity function points, and uncertainties are computed as described in the text. The dotted line shows the Schechter-function fit to the H α luminosity function from the UCM survey (Gallego *et al.* 1995), in the range in which it was determined, converted to the equivalent [O II] luminosity function with the conversion factor $L_{[\text{OII}]} / L_{\text{H}\alpha} = 0.46$, correct for the local Universe (Kennicutt 1992).



Feb 18 10:05:10 1998

Fig. 7.— The dependence of the [O II] 3727 Å luminosity function on redshift, derived from two subsamples of the sample used in this Chapter, split at redshift $z = 0.35$. The upper limit symbols show 68 percent upper limits on the low-redshift subsample, under the conservative assumption that [O II] line luminosity is not correlated with broadband luminosity.



Feb 15 15:23:39 1998

Fig. 8.— The [O II] 3727 Å luminosity and star formation rate densities as a function of redshift are shown with solid circles. The luminosity density is computed as described in the text and the star formation rate density is computed from it using the local calibration (Kennicutt 1992). The horizontal error bars indicate bin widths and the vertical error bars show poissonian uncertainties. Note that neighboring points are based on overlapping data; there are in effect two independent binnings, one centered on 0.2, 0.4, *etc.*, and one on 0.3, 0.5, *etc.* The solid triangle shows the local luminosity density in the H α line from the UCM survey (Gallego *et al.* 1995) converted to the equivalent [O II] luminosity density with the conversion factor $L_{[O II]}/L_{H\alpha} = 0.46$, correct for the local Universe (Kennicutt 1992).